

Spin-lattice coupling and lattice anharmonicity across structural phase transitions in spin-orbit coupled K_2IrBr_6

S. Bhatia¹, A. Ahmad², M. Zeeshan¹, S. Kaur¹, J. K. Anand³, A. Goswami³, B. K. Mani¹, K. Sen^{1,*}

¹Department of Physics, Indian Institute of Technology Delhi, Hauz Khas, New Delhi 110016, India

²Institute of Condensed Matter Physics, Technische Universität Darmstadt,
64289 Darmstadt, Germany

³Department of Materials Science and Engineering, Indian Institute of Technology Delhi, Hauz Khas, New Delhi-110016, India

Abstract:

The interplay between lattice distortions, magnetism, and spin-orbit coupling (SOC) in $5d$ transition-metal halides offers a platform for studying correlated spin-lattice dynamics. Here, we investigate the impact of the temperature-driven structural phase transitions on local spin environments and lattice vibrations in the antiferromagnetic compound K_2IrBr_6 using electron paramagnetic resonance (EPR), Raman scattering, and first-principles calculations. K_2IrBr_6 undergoes two structural transitions at nominal temperatures: cubic-to-tetragonal near 170 K and tetragonal-to-monoclinic at ~ 122 K. EPR reveals persistent spin-spin correlations emerging well above the Néel temperature (12 K), accompanied by strong exchange narrowing and anisotropic g -factors, highlighting the role of SOC and structural symmetry breaking in modifying spin-lattice interactions. Raman scattering identifies phonon anomalies at the transition temperatures, with increasing lattice anharmonicity as symmetry is reduced. While no soft phonons are observed, the systematic enhancement of anharmonic effects suggests that evolving spin correlations may contribute to phonon renormalization. These findings establish K_2IrBr_6 as a model system for investigating coupled spin-lattice effects in SOC-driven materials.

I. Introduction

The interplay between lattice distortions, magnetism, and spin-orbit coupling (SOC) in $5d$ transition metal compounds has garnered significant attention due to its role in stabilizing exotic quantum phases [1,2]. Unlike their $3d$ counterparts, $5d$ materials exhibit a delicate competition between SOC, Coulomb interactions, and crystal field effects, often leading to unconventional magnetic and lattice dynamics [3–5]. Understanding how structural distortions influence both spin and lattice degrees of freedom is crucial for unraveling emergent behaviors in SOC-driven systems, including nontrivial spin-lattice interactions and phonon anomalies [1,6].

Materials such as Sr_2IrO_4 and Na_2IrO_3 have demonstrated that strong SOC can stabilize $j_{\text{eff}} = 1/2$ electronic states, resulting in novel magnetic ground states [7,8]. More recently, perovskite and antiferromagnetic-type iridates have emerged as new platforms to explore spin-lattice coupling, with examples such as Ba_2YIrO_6 [9] and K_2IrCl_6 [10] revealing intricate connections between structural distortions and electronic or phononic properties. The antiferromagnetic family (K_2IrX_6 , $X = \text{Cl, Br, I}$) is particularly interesting because its face-centered cubic (FCC) lattice provides a nearly ideal realization of $j_{\text{eff}} =$

$1/2$ magnetism. In these materials, structural transitions involving octahedral tilts and distortions significantly impact phonon behavior, exchange interactions, and magnetism, with K_2IrCl_6 recently proposed as a candidate for a nodal-line spin-liquid state [11].

K_2IrBr_6 presents an excellent opportunity to investigate the coupling between spin, lattice, and structural symmetry changes. It undergoes successive structural transitions from a high-symmetry cubic phase to a tetragonal phase at 170 K and further to a monoclinic phase at 122 K, driven by cooperative deformations, tilts, and rotations of the IrBr_6 octahedra [12]. These transitions coincide with a change from a high-temperature paramagnetic phase to an antiferromagnetic state below $T_N \approx 12$ K, suggesting an intricate coupling between lattice symmetry breaking and spin dynamics. However, to date, no experimental studies have explicitly explored the spin-lattice coupling or the dynamic interplay between lattice vibrations and spin correlations in this system. This gap leaves open key questions about how structural symmetry breaking influences spin dynamics and whether spin correlations actively contribute to modifications in lattice properties.

In this work, we explore for the first time the spin and lattice dynamics of K_2IrBr_6 using electron paramagnetic resonance (EPR) and Raman scattering, providing direct experimental insight into the interplay between evolving

* kaushik.sen@physics.iitd.ac.in

spin correlations, structural symmetry breaking, and lattice vibrations. EPR results reveal persistent spin-spin correlations emerging below the cubic-to-tetragonal transition, suggesting that symmetry reduction enhances exchange interactions and modifies spin-lattice coupling. Complementary Raman studies reveal phonon anomalies at the structural transition temperatures, with increasing lattice anharmonicity as symmetry is reduced. While no soft phonons were observed, the strong phonon-lattice coupling and the systematic enhancement of anharmonicity suggest that lattice distortions strongly influence phonon renormalization. The possibility that evolving spin correlations further modify lattice anharmonicity introduces an additional fundamental aspect to the observed behavior, highlighting the deep interconnection between spin and lattice degrees of freedom.

By establishing K_2IrBr_6 as a model system for SOC-driven spin-lattice coupling, this study provides new insights into the role of structural distortions in shaping both magnetic and vibrational properties. The findings indicate that antiferromagnetic-type iridates provide an important testbed for exploring correlated spin-lattice dynamics, as their structural transitions and well-defined $j_{\text{eff}} = 1/2$ states allow for a controlled investigation of SOC-driven interactions. The results suggest that similar coupled dynamics may be present in other antiferromagnetic-type iridates, motivating further studies on their potential for hosting unconventional magnetic phases.

II. Methods

A. Experiments

We performed experiments on commercially available pristine polycrystalline K_2IrBr_6 (KIB) (Ir 25.4% min) from Alfa Aesar. We did x-ray diffraction (XRD) experiments at 13, 140, and 300 K for structural characterization. Specifically, we performed powder XRD using a Malvern Panalytical Empyrean Series 3 XRD diffractometer with $\text{Cu-K}\alpha$ radiation ($\lambda = 1.54 \text{ \AA}$). The symmetric $\theta - 2\theta$ scans were performed between $2\theta = 10^\circ$ and 80° . With the help of Rietveld refinement of the XRD data, we were able to confirm cubic-to-tetragonal phase transition. However, our limited resolution did not enable us to observe tetragonal-to-monoclinic phase transition, which was earlier confirmed by the high resolution XRD experiment with synchrotron radiation ($\lambda = 0.4001 \text{ \AA}$) in ref. [12].

DC magnetization measurements were carried out using a Quantum Design made MPMS-3 setup. For measurements, we wrapped 15 mg polycrystalline sample in a Teflon tape and placed it inside a straw that is attached

to the sample rod via an adapter. We punctured the straw in several places near the sample to facilitate purging inside the helium gas environment in order to reduce the trapped air inside the sample, which often gives rise to an unwanted signal around 50 K. For data acquisition, we cooled from 300 to 2 K under an applied magnetic field of 0.1 tesla and recorded the data while warming up to 300K.

The temperature-dependent Electron paramagnetic Resonance (EPR) spectra were recorded using Bruker Biospin spectrometer (A300-9.5/12/S/W). The powder was kept in the quartz sample tube, which was placed in the EPR cavity for measurement. The data were recorded at the microwave frequency of 9.39 Hz at a power of 1 mW. The data were accumulated seven times at each temperature for better data quality. EPR results were recorded at several temperatures while warming up from 100 K to 300 K.

We recorded Raman spectra as a function of temperature using a WiTec alpha300 R Raman spectrometer and continuous liquid N_2 cryostat. We used a laser excitation of 532 nm through a microscope objective of 50x onto polycrystalline powder of K_2IrBr_6 . To minimize Rayleigh scattering contribution, we used a filter. Effectively, we measured Raman spectra over the energy range of 50 to 500 cm^{-1} with a diffraction grating of 600 grooves/mm. In all the measurements, we kept a low laser power of 1.4 mW to minimize laser-induced heating. To acquire Raman spectra at several temperatures, we first cooled down the sample to the base temperature 77 K. The data at subsequent temperatures were recorded after warming up to the required temperature upon reaching proper thermalization.

B. Computational details

The structural, vibrational, and symmetry properties of KIB were investigated using density functional theory (DFT) and density functional perturbation theory (DFPT) as implemented in the Vienna Ab initio Simulation Package (VASP). The initial structural relaxations were carried out for the cubic, tetragonal, and monoclinic phases of KIB. A plane-wave cutoff energy of 500 eV was employed, and the forces on all atoms were minimized to converge below 0.01 eV/ \AA . A Γ -centered k -point mesh of $4 \times 4 \times 4$ was used for these calculations to ensure accurate results for subsequent simulations. Symmetry-preserving supercells were generated to accommodate finite-displacement calculations. For the cubic phase, a $2 \times 2 \times 1$ supercell containing 144 atoms was constructed. Similarly, $2 \times 2 \times 1$ supercells with 72 atoms each were used for the tetragonal and monoclinic phases. The dynamical matrix was computed using finite-displacement methods. This

involved small displacements of atoms 0.01 Å within the supercell, and the resulting forces were used to calculate phonon frequencies. The Phonopy package was employed to determine phonon eigenfrequencies and eigenvectors. These calculations were performed for high-symmetry points in the Brillouin zone to examine the phonon dispersion and mode classification. A detailed symmetry analysis was conducted to identify Raman- and IR-active phonon modes for each phase. This step provided insight into the vibrational properties and their potential experimental observability.

III. Results and discussions

A. Structural properties

As mentioned earlier, we confirm the cubic-to-tetragonal phase transition in KIB using XRD, albeit with limited resolution. However, for the completion of the paper in the context of our results, we discuss the relevant structural properties based on ref. [12], as these structural transitions play a crucial role in understanding the observed spin and lattice dynamics.

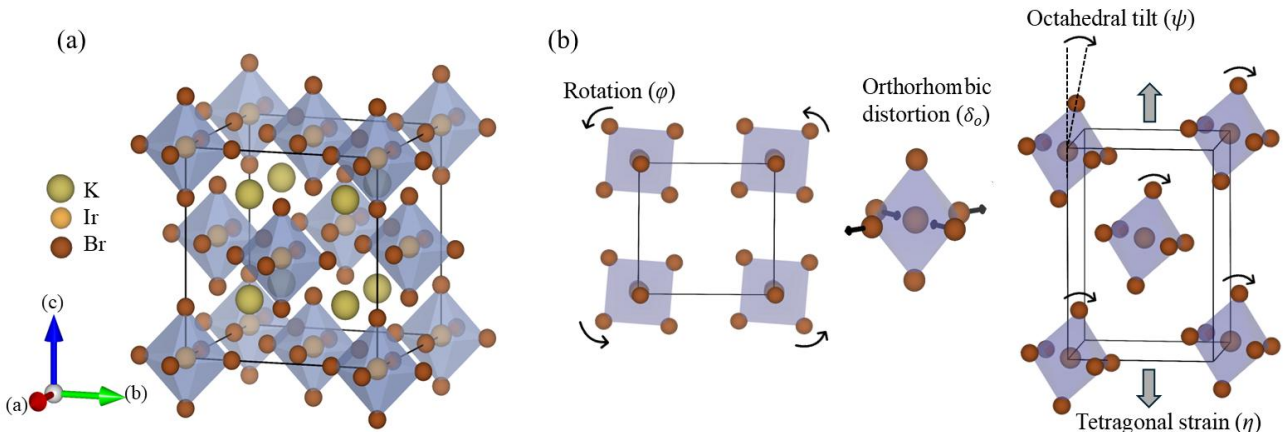


FIG. 1. (a) Schematic diagram of crystal unit cell of K_2IrBr_6 based on the crystal structure at room temperature. (b) A summary of relevant distortions in KIB: Octahedral rotation (φ) and tilt (ψ), orthorhombic distortions (δ_o), and tetragonal strain (η). The figure is adapted from ref. [12].

Crystallographically, KIB has a cubic structure, specifically adopting a face-centered cubic arrangement with the Ir^{4+} ions at the vertices and faces of the cubic unit cell, as shown in FIG. 1(a). In this structure, Ir^{4+} ions sit at the center of the octahedra formed by Br^- ions. The octahedra are separated by K^+ ions, which ensures that there is no corner or edge-sharing of atoms in the octahedra. Although the structure is cubic at room temperature, rotations, tilts, and deformations of the octahedra lead to different types of symmetry lowering structures, as reported in ref. [12]. Specifically, high-

resolution synchrotron x-ray diffraction experiments obtained that KIB undergoes a room-temperature cubic to tetragonal phase transition below ~ 170 K, and further tetragonal to monoclinic transition below ~ 122 K.

FIG. 1(b) summarizes the various structural distortions in KIB, including octahedral rotations (φ), which correspond to in-plane rotations of the $IrBr_6$ octahedra, and octahedral tilts (ψ), which emerge in the monoclinic phase as a tilt relative to the c -axis. Tetragonal strain (η) reflects an elongation of the crystal lattice along one of the principal axes, while maintaining constant Ir-Br bond lengths. Orthorhombic deformation (δ_o) describes bond length variations within the octahedron, which become more pronounced in the lowest-temperature phase. These distortions affect the crystal symmetry and influencing the magnetic characteristics of the material.

B. Magnetic properties

FIG. 2 shows DC magnetic susceptibility (χ) of 15 mg polycrystalline KIB under a magnetic field of 0.1 T. χ increases with decreasing temperature down to 16 K,

indicating a paramagnetic state. However, the continuous drop in χ below ~ 16 K towards low temperatures is an indication of the occurrence of antiferromagnetic (AF) order with $T_N \cong 16$ K which is close to the reported value of 12 K [12]. In the inset, we plotted the temperature derivative of the inverse susceptibility ($d\chi^{-1}/dT$) between 150 and 220 K. The distinct peak around 184 K in ($d\chi^{-1}/dT$) versus T plot has been associated with the first-order cubic-to-tetragonal phase transition. This is consistent with the earlier report [12].

χ vs. T well above the cubic-to-tetragonal structural transition (184 K) in the paramagnetic phase was fitted with the following Curie-Weiss formula as mentioned in equation 1.

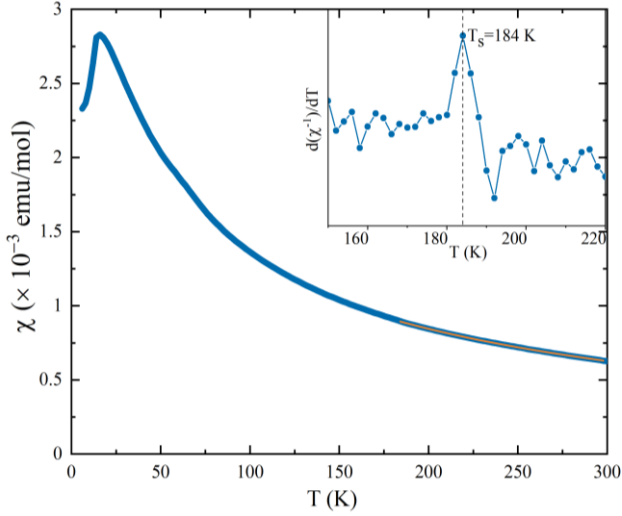


FIG. 2. DC magnetic susceptibility (χ) versus temperature for polycrystalline K_2IrBr_6 ($\mu_0 H = 0.1$ T). The inset shows the $d(\chi^{-1})/dT$ in the vicinity of cubic to tetragonal transition.

$$\chi = \chi_0 + \frac{C}{T - \theta_{CW}}, \quad (1)$$

where χ_0 is the temperature-independent diamagnetic contribution, C is the Curie constant and θ_{CW} is the Curie-Weiss temperature. Here, $C = \frac{N_A \mu_{eff}^2}{3k_B}$, where N_A is Avogadro's number, μ_{eff} is the effective paramagnetic magnetic moment, and k_B is the Boltzmann constant. The fitting yields $\chi_0 = -9.6 \times 10^{-4}$ emu/mol, which can be compared with χ_0 for other Ir^{4+} compounds [10], [13]. The fitted value of Curie constant, $C = 0.2438$ emu K/mol, and $\theta_{CW} = -88.6$ K, which are in close agreement with the reported values in ref. [12]. Further, we obtained $\mu_{eff} = 1.38 \mu_B$ per Ir^{4+} ion, which is close to the expected magnetic moment of $1.73 \mu_B$ for $j_{eff} = 1/2$ and $g = 2$.

C. Local magnetism with electron paramagnetic resonance

We performed electron paramagnetic resonance (EPR) experiment as a function of temperature to probe the impact of structural phase transitions on the local magnetic environment and spin dynamics above T_N . FIG. 3 shows derivative EPR spectra ($\frac{dP}{dH}$ (P is the integral EPR intensity and H is the applied magnetic field) of polycrystalline KIB at several temperatures, from 300 to 100 K. At 300 K, in the cubic phase, two clear substructures are visible in the EPR spectrum, indicated by the dashed blue and black vertical lines. The substructure

indicated by the blue dashed line is found to be the most sensitive to varying temperature. In particular, the mode shifts towards higher magnetic fields as we approach from the cubic to the tetragonal phase. Overall, the spectra get narrower towards low temperatures, which allows us to observe more substructures in the spectra. For instance, a curvature change appears around ~ 5000 Oe at low temperatures, as indicated by an arrow in the 100 K spectrum. It seems that such a change in curvature begins to emerge already at 150 K (tetragonal phase). Certainly, the reduction in crystal symmetry from cubic to tetragonal, i.e. increased non-cubic distortions paves the way for the observation of this mode. Further, this high-field mode is significantly broader than the remaining substructures in the spectra. Such a broad structure possibly consists of multiple unresolved fine substructures due to hyperfine interactions associated with the nuclear spins of Ir ($I = 3/2$) and Br ($I = 3/2$). In covalent complexes of $[\text{IrBr}_6]^{2-}$, unresolved broad paramagnetic resonances

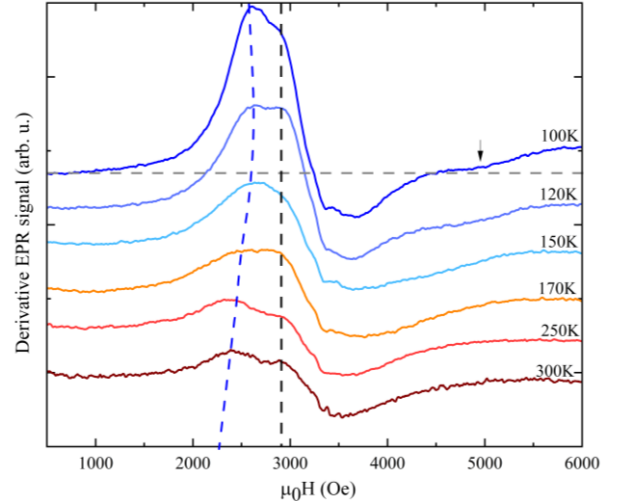


FIG. 3. Derivative EPR spectra of polycrystalline KIB.

were observed, particularly when the applied magnetic field is not aligned with one of the crystallographic principle axes [14], as is the case here, where polycrystalline KIB was measured.

The presence of multiple substructures in $\frac{dP}{dH}$ confirms that $j_{eff} = 1/2$ spins of Ir^{4+} ions sit in a magnetically anisotropic environment. This pronounced anisotropy stems from persistent local distortions, including dynamic and static rotations of the IrBr_6 octahedra, even in the nominally cubic phase, as confirmed by recent structural investigations and the presence of non-cubic crystal fields [12]. Such rotations disrupt ideal cubic symmetry and induce local variations in the crystal field, splitting the t_{2g} orbitals. Consequently, the low-lying degenerate $j_{eff} =$

3/2 is split into two levels, enabling mixing between the paramagnetic $j_{\text{eff}} = 1/2$ and components of the $j_{\text{eff}} = 3/2$ state. This mixing introduces additional diversity to the magnetic environments of the Ir^{4+} ions, leading to the observed complexity in the EPR response. In contrast, for a magnetic isotropic system with uniform crystal-field effects, we expect a single EPR mode (single Lorentzian-derivative profile), corresponding to a unique g -factor when polycrystalline sample is measured [14]. Our results may appear contradictory with the finding of isotropic g -factors for the isostructural compounds $(\text{NH}_4)_2\text{IrCl}_6$ and K_2IrCl_6 with cubic symmetry [15]. However, the greater isotropy observed in the covalent $[\text{IrCl}_6]^{2-}$ complexes compared to $[\text{IrBr}_6]^{2-}$ can be attributed to larger electron affinity and smaller ionic radius of chloride ions relative to bromide ions. These differences lead to smaller and more symmetric $[\text{IrCl}_6]^{2-}$ octahedra compared to the larger and more distorted $[\text{IrBr}_6]^{2-}$ octahedra. The pronounced anisotropic g -factor observed in our study reflects the strong spin-lattice coupling and substantial spin-orbit interaction inherent to the Ir^{4+} ions. The robust spin-orbit coupling (SOC) in $5d\text{-Ir}^{4+}$ ensures that $j_{\text{eff}} = 1/2$ spins are not truly free but remain strongly entangled with the lattice through their orbital degrees of freedom. This inherent anisotropy is a hallmark of SOC-driven systems, where spin-orbit interactions induce significant deviations from ideal isotropy [16,17].

After qualitative discussion on the anisotropic g -factors, we now quantify them and track their temperature dependence and the lineshape of the corresponding EPR substructures. As mentioned earlier, the substructure indicated by the blue dashed line in FIG. 3 shows a relatively strong temperature dependence. Further, $\frac{dP}{dH}$ at 100 K is significantly asymmetric with respect to the spectrum at 300 K as shown by the horizontal dashed line in FIG. 3. To extract the lineshape parameters, i.e., resonant field ($\mu_0 H_r$), linewidth ($\mu_0 \Delta H$), and asymmetric spectral weight, the EPR spectra were fitted with the sum of the derivatives of symmetric (L_S) and anti-symmetric (L_A) Lorentzian profiles.

The best fits were obtained when four modes are considered for the data at or below 150 K, while three modes are enough for the spectra above 150 K.

We used the following functions for fitting:

$$I_{\text{EPR}} = \frac{1}{\mu_0} \left(\sum_{i=1}^4 \frac{\partial}{\partial H} (L_{S,i} + L_{A,i}) \right) \quad (2)$$

, where $\mu_0 H$ is the applied magnetic field and the summation runs for the four modes. L_S and L_A are defined as:

$$L_S = S \frac{\Delta H^2}{\Delta H^2 + (H - H_r)^2}, \quad (3)$$

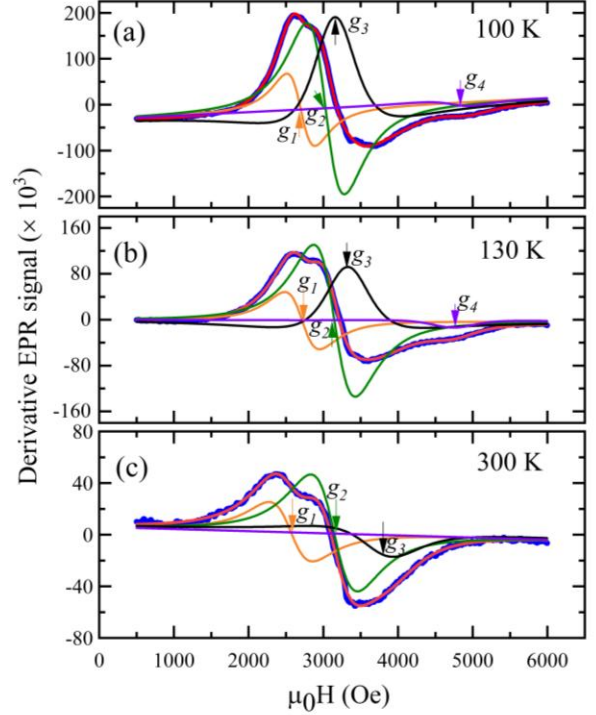


FIG. 4. Representative fitting to the EPR spectra of polycrystalline KIB using eq. (2) at (a) 100, (b) 130, and (c) 300 K. Solid blue symbols are the raw data, and the solid red lines are the best fits. The substructure components are shown by solid lines, where orange: g_1 , green: g_2 , black: g_3 , and violet: g_4 .

$$L_A = A \frac{\Delta H^2 (H - H_r)}{\Delta H^2 + (H - H_r)^2} \quad (4)$$

, where S and A are the spectral weights for the symmetric and anti-symmetric Lorentzian profiles, respectively.

FIG. 4(a), (b) and (c) show representative fits to the EPR spectra at three selected temperatures of 100, 130, and 300 K, respectively. As shown in FIG. 4, the EPR spectra, particularly the g_3 -substructure (as indicated by arrow) gradually becomes more asymmetric and narrow with temperature reduction. This will be further discussed in the context of FIG. 6(b).

In accordance with the fitting results, we mark the resonant fields by arrows on the EPR spectra in FIG. 4. We mark the modes as g_1 , g_2 , g_3 , and g_4 from low to high magnetic fields. g_4 is associated with the broad mode that possibly stems from the hyperfine interactions, as discussed earlier. The remaining g -factors correspond to (g_x, g_y, g_z) . Since we measure polycrystalline KIB, we cannot confirm g -values along crystallographic x , y , and z -axes.

FIG. 5 shows $\mu_0 H_r$ and g -factors for all the modes as a function of temperature. The g -factors were evaluated using the relationship $g = (h\nu/\mu_B \mu_0 H_r)$, where h is the Planck's constant, μ_B is the Bohr magneton, and $\nu = 9.39$ GHz is the microwave frequency for X-band [18].

We marked cubic, tetragonal, and monoclinic phases in FIG. 5 following the transition temperatures reported in ref. [12]. In the cubic phase, g_1, g_2 , and g_3 deviate significantly from the spin-only value 2.003 [19], a direct result of the strong spin-orbit interaction in Ir^{4+} ions. This SOC entangles spin and orbital degrees of freedom, shaping the electronic and magnetic properties of the system [20]. In the cubic phase, g_1, g_2 and g_3 show very subtle temperature dependence. Upon further cooling, g_1 sharply decreases after entering the tetragonal phase with the temperature onset of ~ 170 K. Below 150 K, the change of g_1 as a function of temperature is almost temperature independent. On the other hand, g_2 -mode is not as strongly temperature-dependent as the g_1 -mode is. However, g_2 also shows non-monotonic temperature dependence upon entering the tetragonal phase. In particular, g_2 shows a slight increment while cooling down through several phases. The impact of structural phase transitions on g_3 -mode is the strongest. g_3 significantly increases as the system enters the tetragonal phase and then the monoclinic phase. g_4 sharply decreases as we approach the tetragonal phase from the cubic phase. Further, it slightly drops in the monoclinic phase towards low temperatures.

We qualitatively relate the structural changes as a function of temperature, reported in ref. [12], to the observed temperature dependence of g_1, g_2 , and g_3 . All three g -factors exhibit weak and similar temperature dependence in the cubic phase. Upon transitioning to the tetragonal phase, g_1 decreases sharply, while g_3 shows a pronounced increase. This behavior may correspond to the onset of static cooperative octahedral rotations (φ) as well as octahedral tilting (ψ) and tetragonal strain (η), as reported in ref. [12] and illustrated in FIG. 1(b). These structural distortions result in a disparity between the azimuthal and apical Ir-Br bond lengths, which amplify the anisotropy. In the monoclinic phase, orthorhombic distortions (δ_o , i.e. differences between azimuthal Ir-Br bond lengths in [12]) and octahedral tilts (ψ in ref. [12]) further lower the symmetry, leading to continued changes in g_2 and g_3 . These temperature-dependent g -factor variations strongly correlate with the structural transitions from cubic to tetragonal to monoclinic, highlighting the critical role of spin-lattice coupling in shaping the magneto-structural properties of KIB.

Finally, we comment on the hyperfine coupled g_4 mode. This mode is absent in the high-symmetry cubic phase but emerges deep within the tetragonal phase and persists upon further cooling through the tetragonal-to-monoclinic transition. The absence of g_4 in the cubic phase suggests that it is symmetry-forbidden in environments with high structural symmetry. Its appearance in the tetragonal and monoclinic phases

correlates with the onset of structural distortions that break cubic symmetry, such as cooperative octahedral rotations, tetragonal strain, and tilts, which lift the symmetry-constraints and allow the mode to become observable. The gradual decrease in g_4 with cooling may reflect the evolution of hyperfine interactions as the lattice distortions stabilize and the local environment of Ir^{4+} ions becomes more anisotropic. This behavior underscores the sensitivity of the g_4 mode to local lattice symmetry and highlights again the coupling between spin and lattice degrees of freedom in KIB.

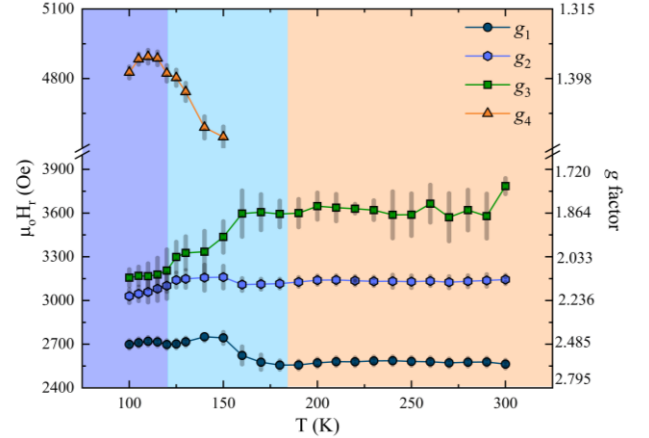


FIG. 5. Temperature dependence of the resonance fields ($\mu_0 H_r$) and the corresponding g -factors for the four EPR modes. The fourth EPR mode (g_4) is negligible above 150 K.

We now turn to the linewidth of the modes, focusing on the two most intense modes g_1 and g_2 . Their linewidths are nearly temperature-independent above ~ 170 K in cubic phase but sharply decrease with reducing temperature below 170 K, as shown in FIG. 6(a). This behavior can be understood in terms of the interplay of spin relaxation mechanisms and structural transitions. In the high-symmetry cubic phase, the dynamic rotations of IrBr_6 octahedra dominate [12], creating a fluctuating magnetic environment. These rapid lattice distortions average out local field inhomogeneities, suppressing efficient spin-lattice relaxation via acoustic phonons (Orbach process). Expectedly weak spin-spin correlations at high temperatures in this phase further contributes to the temperature-independent linewidth, consistent with a dynamically disordered lattice. In contrast, the sharp drop in linewidth below 170 K coincides with the cubic-to-tetragonal phase transition and the emergence of static structural distortions, such as cooperative octahedral rotations (φ) and tetragonal strain (η) [12]. These structural changes stabilize the lattice and enhance spin-spin correlations, reducing magnetic field inhomogeneities. This behavior is characteristic of exchange narrowing, a phenomenon where strong spin-

spin interactions reduces local magnetic field variations, leading to narrower linewidths [21,22]. As the system undergoes further symmetry lowering in the tetragonal and monoclinic phases, the effect of exchange narrowing becomes increasingly pronounced, reflecting the progressive strengthening of spin-spin correlations with reduced lattice symmetry. The temperature-dependent linewidth evolution reveals how structural distortions stabilize spin correlations, reinforcing the link between spin and lattice degrees of freedom.

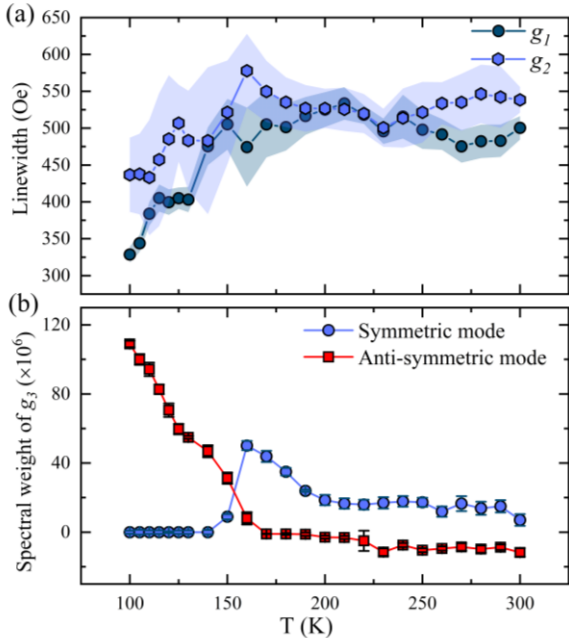


FIG. 6. (a) Linewidth of two most prominent modes (g_1 and g_2) of KIB as a function of temperature. (b) Spectral weight of symmetric and anti-symmetric lorentzian profile of g_3 mode.

We now discuss an intriguing result related to the symmetry of the g_3 mode's spectral weight. From the fitting, the g_1 and g_2 modes are found to be symmetric. However, as shown in FIG. 6(b), the symmetric component of the g_3 mode sharply drops to a negligible value upon entering the tetragonal phase, while the anti-symmetric component emerges and evolves continuously with decreasing temperature, down to the lowest recorded temperature of 100 K. This temperature-dependent evolution of the g_3 mode below the cubic-to-tetragonal phase transition highlights the significant role of spin-lattice coupling in these phases. The origin of the anti-symmetric component in the tetragonal and monoclinic phases appears to be intrinsic, as it emerges below the cubic phase transition and cannot be attributed to experimental artifacts, such as instrumental dispersion effects. A plausible explanation is that pronounced magnetic anisotropy, enhanced by strong SOC in Ir^{4+} ions, breaks the symmetry of spin relaxation pathways, resulting

in an anti-symmetric EPR line shape. Another plausible mechanism involves the non-diagonal elements of the dynamic susceptibility tensor, which are essential in systems with anisotropic interactions. Such interactions, including spin-orbit coupling and the Dzyaloshinskii-Moriya (DM) interaction, are known to produce non-collinear or non-uniform spin configurations. The DM interaction, inherently asymmetric due to SOC, becomes symmetry-allowed in lower-symmetry tetragonal and monoclinic phases, while being prohibited in the high-symmetry cubic phase [3], [16]. Its activation below the cubic-to-tetragonal phase transition may contribute to the observed anti-symmetric EPR line shape in these phases. This transition-driven emergence of the DM interaction highlights the interplay between spin-orbit coupling, spin-lattice coupling, and symmetry-breaking distortions, offering a deeper insight into the complex spectral evolution of the g_3 mode in KIB.

The main findings from the EPR study indicate that spin dynamics in KIB closely follow structural transitions, with significant changes in g -factors and linewidths across phase boundaries. Spin-spin correlations emerge below 170 K, well above the Néel temperature, indicating the influence of structural distortions on magnetic interactions. The asymmetric EPR line shape in the tetragonal and monoclinic phases reflects the role of spin-orbit coupling and structural distortions in modifying spin relaxation processes.

D. First-principles calculations

To investigate how lattice dynamics evolve across structural transitions, we first establish the expected Raman phonon modes at zone-center through first-principles calculations, as no prior Raman studies exist on KIB. Group theory analysis for the cubic phase (space group $\text{Fm}\bar{3}\text{m}$) yields one A_{1g} , one E_g , and two T_{2g} phonon modes under the point group of O_h . Reduction of lattice symmetry from cubic to tetragonal (P4/mnc) and further to monoclinic ($\text{P2}_1/\text{n}$) gives rise to increased numbers of phonon modes. The tetragonal phase yields three A_{1g} , three B_{1g} , two B_{2g} , and six A_g modes under the point group of D_{4h} . In the monoclinic phase, the phonon modes are twelve A_g and twelve B_g under the point group of C_{2h} . These are summarized in Table I for brevity.

We determined the energy of the phonon modes and their Eigen displacements using first-principle lattice dynamics calculations based on density functional perturbation theory (DFPT). Table II lists the phonon mode energies for the cubic phase (phonon mode energies for the tetragonal and monoclinic phases are given in Appendix A for completeness). The corresponding Eigen

displacement vectors are shown in FIG. 7(a)-(d). The T_{2g} modes in cubic KIB include two distinct displacement patterns. The external T_{2g} mode (61.6 cm^{-1}) represents the relative motion of K ions with respect to the nearly stationary IrBr_6 octahedra. This motion resembles a lattice-breathing effect, with the K-atoms oscillating within the framework defined by the rigid octahedra. The internal T_{2g} mode (108.3 cm^{-1}) involves the scissoring motion of the Br-atoms within the IrBr_6 octahedra. These vibrations tangentially displace the Br-atoms, causing a twisting or shearing motion of the octahedra without significantly

altering the bond lengths between the Ir- and Br-atoms. The E_g mode (189.8 cm^{-1}) involves symmetric stretching of opposite Br-atoms towards or away from the central Ir atom. This motion introduces transient distortions in the IrBr_6 octahedron, leading to dynamic tetrahedral strains without strictly preserving the ideal octahedral symmetry. The A_{1g} mode (222.4 cm^{-1}) corresponds to the symmetric stretching of the Br atoms in the IrBr_6 octahedra, with all Br atoms moving radially, in phase, towards or away from the central Ir atom, preserving the octahedral symmetry.

Table I. Raman-active optical phonon mode symmetries at zone-center for cubic, tetragonal, and monoclinic phases.

Structure Point Group	Cubic O_h	Tetragonal D_{4h}	Monoclinic C_{2h}
Γ_{Raman}	$A_{1g}+E_g+2T_{2g}$	$3A_{1g}+3B_{1g}+2B_{2g}+6E_g$	$12A_g+12B_g$

Table II. Comparison of the calculated and experimental frequencies for Raman phonon modes in cubic phase of K_2IrBr_6 .

Γ_{Raman}	$\omega_{\text{cal}} (\text{cm}^{-1})$	$\omega_{\text{exp}} (\text{cm}^{-1})$	$\Delta\omega = \frac{\omega_{\text{cal}} - \omega_{\text{exp}}}{\omega_{\text{cal}}} \times 100$ (%)
T_{2g}	61.6	71.3	15.7
T_{2g}	108.3	107.2	1.01
E_g	189.8	170.6	10.1
A_{1g}	222.4	208.3	6.33

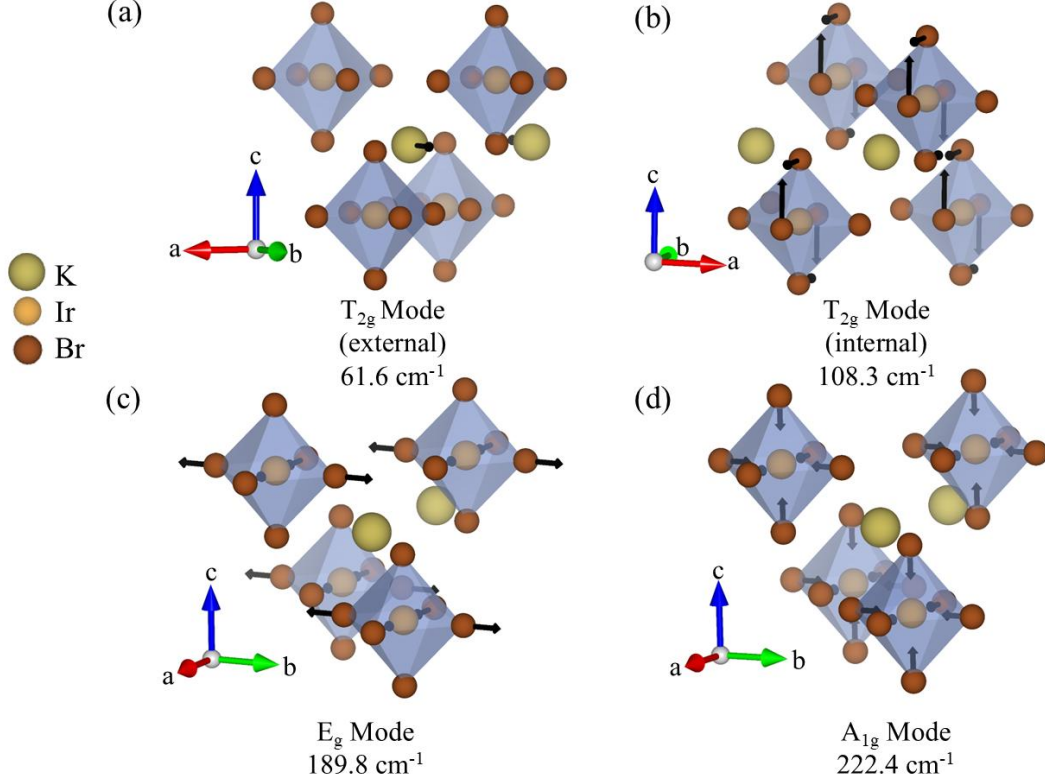


FIG. 7. Eigen displacement vectors for the four Raman-active phonon modes in cubic symmetry of KIB. (a) T_{2g} (external), (b) T_{2g} (internal), (c) E_g , and (d) A_{1g} .

E. Temperature-dependent lattice dynamics

FIG. 8 shows unpolarized Raman spectra of KIB at several temperatures starting from 77 to 300 K. The spectra show three prominent modes at 107.2, 170.6, and 208.3 cm^{-1} at room temperature. In addition, a broad and weak mode is also observed around 71.3 cm^{-1} . From unpolarized Raman scattering experiments alone, we cannot assign the mode symmetries. However, the proximity of these modes with the calculated phonon mode energies, as listed in Table II, allows us to assign the mode symmetry. Specifically, the modes at 71.3, 107.2, 170.6, and 208.3 cm^{-1} are T_{2g} (external), T_{2g} (internal), E_g , and A_{1g} , respectively. The deviation of the calculated phonon mode energy from the experimental values is nominal, varying from 1 to 16 % depending on the modes. This testifies to the reasonably high accuracy of our calculations that facilitates the mode assignment.

We now focus on the Raman spectra at low temperatures, especially across the cubic-to-tetragonal and tetragonal-to-monoclinic phase transitions. According to group theory analysis (Table I) and first-principles calculations of phonon energies for the low-temperature phases (Appendix A), we expect additional phonon modes in the low-temperature Raman spectra due to reduced

crystallographic symmetry. However, our Raman spectra do not reveal any extra peaks that would correspond to new phonon modes. The absence of new phonon modes at low temperatures, despite structural transitions confirmed by XRD, is likely due to weak Raman activity of these modes. First-principles calculations predict additional phonon

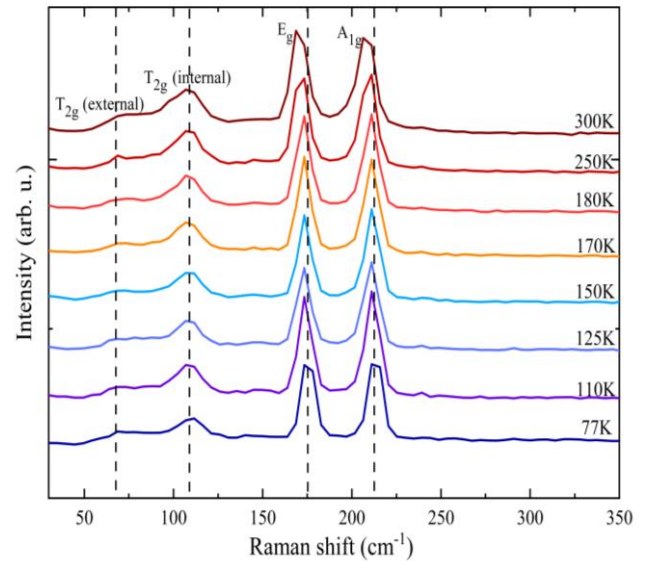


FIG. 8. Unpolarized Raman spectra of KIB at several temperatures.

modes in the reduced symmetry phases, but their contributions to the polarizability tensor may be too small to detect. This is consistent with reports on isostructural compounds like K_2IrCl_6 [23] and K_2ReCl_6 [24], where symmetry-lowered modes show low intensity.

Additionally, Raman spectroscopy likely probes the global structure, as phonon modes originate from collective vibrational waves spanning over the bulk material. Previous studies suggest that Raman scattering may not fully resolve local distortions if their effect on the global symmetry is averaged out [24,25]. As a result, strong signals of the parent cubic phase modes can overshadow these weak modes, while anharmonicity-induced broadening may further obscure them.

To underline the impact of structural transitions on the phonon modes, we require the temperature dependence of phonon mode energies and the linewidths. For this purpose, we fit the Bose-factor corrected Raman spectra with three Lorentzian profiles for the three most prominent modes. FIG. 9(a)-(f) shows the fitting results, i.e., temperature dependences of phonon mode energies and

linewidths (full width at half maxima, FWHM). Broadly, all three modes show hardening towards low temperatures, i.e., mode energy (Raman shift) increases with decreasing temperature, as shown in FIG. 9(a)-(c). However, a prominent anomaly in terms of phonon energy jump can be observed at ~ 125 K for the two most intense modes E_g (FIG. 9(b)) and A_{1g} (FIG. 9(c)). In conformation with phonon hardening towards low temperature, the phonon linewidths decrease with decreasing temperature. However, such linewidth reduction is not monotonic in temperature. Linewidths are weakly temperature-dependent down to 125 K but exhibit strong reductions below 125 K.

Regular phonon mode energy and linewidth as a function of temperature follows the symmetric anharmonic phonon decay model, which is famously known as the Klemens model [26,27]. The model describes phonon decay as an anharmonic process where an optical phonon decays into two acoustic phonons with opposite momentums. Anharmonic lattice interactions broaden phonon linewidths with increasing temperature,

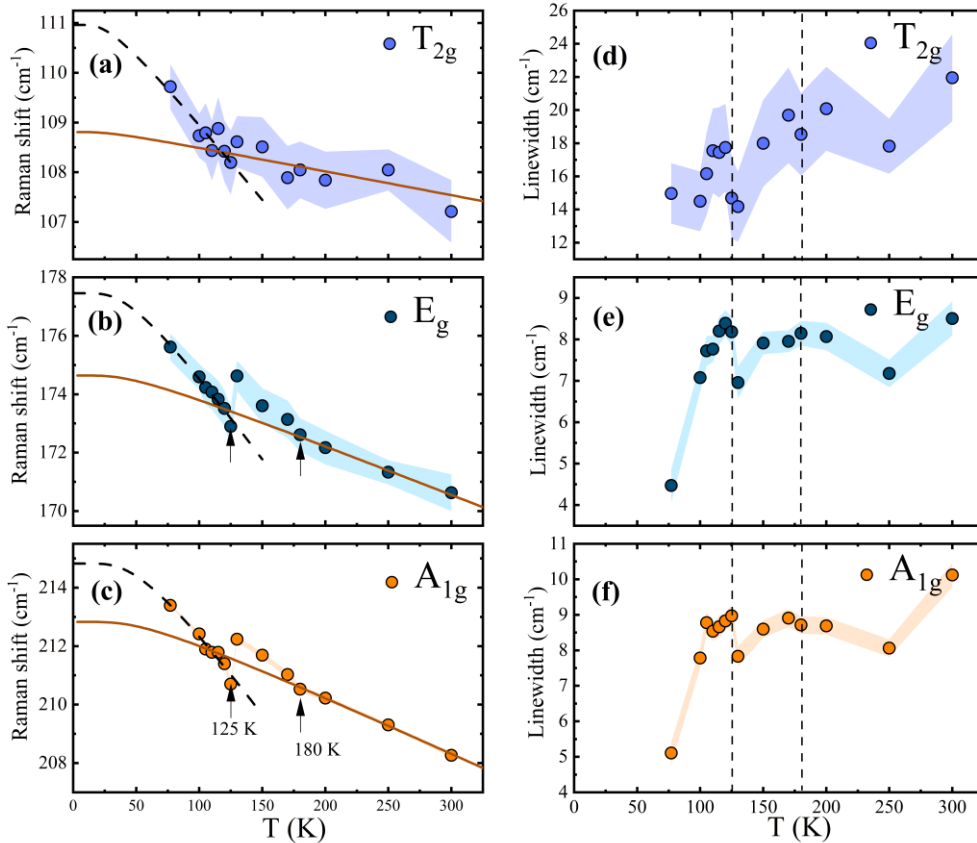


FIG. 9. (a)-(c) Raman shift as a function of temperature (symbols) for T_{2g} (internal), E_g , and A_{1g} modes, (d)-(f) The corresponding linewidths as a function of temperature. The solid black line and the dotted red line through the data in (a)-(c) are the best fits according to Klemen's decay model in cubic and monoclinic phase, respectively. The deviations of the Raman shift from the Klemen's decay model are indicated by arrows in (b) and (c). Accordingly, the vertical dotted lines are drawn at the corresponding temperatures in the linewidth vs. temperature plots in (d)-(f).

often in a nearly linear fashion at high temperatures, as described by the Klemens model [28]. This behavior arises from increased phonon-phonon scattering due to the higher phonon population density at elevated temperatures. However, the phonon linewidths of KIB shows a significant departure from this regular trend. According to Klemens model, the phonon frequency (ω) as a function of temperature (T) follows eq. 5.

$$\omega(T) = \omega_0 - C \left(1 + \frac{2}{e^{\hbar\omega_0/k_B T} - 1} \right) \quad (5)$$

where ω_0 is the natural phonon frequency in the absence of any anharmonic lattice interactions, and C is the anharmonic constant that signifies the strength of anharmonic interactions. After carefully analyzing the phonon frequency versus temperature plots for the two most intense phonon modes in FIG. 9(b) and (c), we identified two distinct linear regimes in the phonon energy versus temperature relationship. At high temperatures, we fitted ω -vs.- T data in the range of 180 to 300 K using the Klemens model and extrapolated it to lower temperatures following the same model.

The results show that ω follows the Klemens model from room temperature down to 180 K. However, below 180 K, ω -vs.- T deviates significantly from the model. Specifically, ω hardens towards lower temperatures more than predicted by the model, and upon reaching 125 K, it abruptly softens before increasing almost linearly with decreasing temperature down to our lowest measured temperature of 77 K. Such deviations from the Klemens model are prominent for both the intense E_g and A_{1g} mode.

Interestingly, the cubic-to-tetragonal and tetragonal-to-monoclinic structural phase transitions occur at ~ 170 K and 122 K, respectively [12]. It is, therefore, reasonable to associate the observed phonon anomalies with these structural transitions. This conclusion is further supported by the non-monotonic behaviour of phonon linewidths as a function of temperature, particularly near the structural transition temperatures. Structural transitions often modify lattice symmetry and anharmonic coupling, leading to changes in phonon scattering rates and lifetimes, which manifest as anomalies in the linewidth [29]. The simultaneous anomalies in both phonon energy and linewidth suggest significant alterations in the phonon self-energy during these transitions. Specifically, the real part of the phonon self-energy governs shifts in phonon frequency ω -vs.- T , while the imaginary part determines the linewidth, reflecting changes in phonon damping. These observations highlight the strong impact of structural transitions on the lattice dynamics, altering both the vibrational frequencies and scattering processes within the material.

In the monoclinic phase, the ω -vs.- T behaviour can still be described by the Klemens model, albeit with a stronger anharmonic constant C . The increased anharmonicity is reflected in a steeper ω -vs.- T characteristic, which we attribute to enhanced lattice anharmonicity due to the reduced symmetry in the monoclinic phase. The lower symmetry of the monoclinic phase likely introduces stronger coupling among phonons, which leading to anharmonic effects. Notably, this stronger anharmonicity may also be linked to the enhanced spin-spin correlations observed in the low-temperature phases, as evidenced by the exchange-narrowed linewidths in the EPR data below the cubic-to-tetragonal phase transition that persist into the monoclinic phase. In the monoclinic phase, lower crystal symmetry augments coupling not only among lattice vibrations but also with the spin degrees of freedom, leading to more pronounced deviations from harmonic behaviour. For quantification, we compared the anharmonic constants C for two different phonon decay regimes in the cubic and monoclinic phases in FIG. 10. For all the modes, lattice anharmonicity in the monoclinic phase is greater than in the cubic phase. Overall, our observation suggests that enhanced lattice anharmonicity is closely linked to the reduction in crystallographic symmetry and the onset of spin-spin correlations at low temperatures.

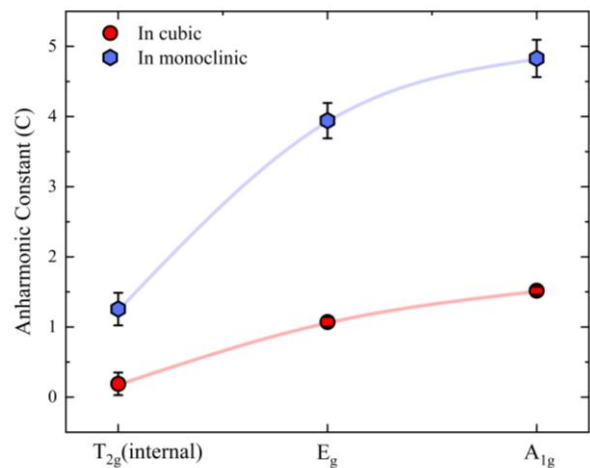


FIG. 10. Anharmonic constant C for cubic and monoclinic phases of KIB, as obtained from the fits with Klemens's phonon decay model.

IV. Conclusion

$K_2\text{IrBr}_6$ serves as a platform to investigate how strongly local magnetization ($j_{\text{eff}} = 1/2$) and lattice vibrational properties are sensitive to the underlying lattice symmetry in the context of structural transitions, low-temperature magnetism, and strong spin-orbit coupling. It undergoes successive structural phase transitions from a high-symmetry cubic phase to a tetragonal phase below

170 K and then to a monoclinic phase below 122 K, driven by cooperative deformations, tilts, and rotations of the IrBr_6 octahedra [12]. These structural changes accompany a transition from a high-temperature paramagnetic state to a low-temperature antiferromagnetic phase below $T_N \sim 12$ K [12].

Electron paramagnetic resonance (EPR) experiments reveal an anisotropic magnetic environment around $j_{\text{eff}} = 1/2$ spins, even in the cubic phase, indicating local non-cubic distortions that persist at high temperatures. This observation is consistent with earlier structural and resonant inelastic x-ray scattering studies, which suggest that local distortions of the IrBr_6 octahedra introduce a non-cubic crystal field even in the nominally cubic phase [12]. The anisotropic g -factors derived from EPR data are distinct from the free-electron value, reflecting the strong spin-orbit coupling (SOC) of the Ir^{4+} ions. Further, due to strong SOC, g -factors exhibit non-monotonic changes as a function of temperature, primarily occurring at the structural transition temperatures.

Interestingly, below the cubic-to-tetragonal transition, the significant narrowing of the EPR linewidth due to exchange narrowing indicates the emergence of persistent spin-spin correlations well above T_N . This suggests that symmetry reduction enhances exchange interactions, facilitating spin correlations in the nominally paramagnetic phase. Additionally, the onset of these correlations coincides with structural distortions, indicating that spin-lattice coupling plays a crucial role in mediating exchange interactions. The structural distortions in the tetragonal phase likely stabilize these correlations, highlighting a strong interplay between lattice symmetry breaking and spin dynamics in this spin-orbit coupled system.

A related compound, K_2IrCl_6 , has been argued to host a nodal-line spin-liquid phase, where strong spin-orbit coupling and exchange frustration give rise to extended spin correlations in the absence of conventional order [10,11]. While K_2IrBr_6 has not yet been explored in this context, the presence of persistent correlations and lattice distortions suggests it may exhibit similar correlated spin dynamics, warranting further study [2].

Raman scattering experiments confirm the presence of all expected phonon modes in the cubic phase, with their symmetries assigned through first-principles lattice dynamics calculations. Despite structural transitions, no new phonon modes appear at low temperatures, and no soft phonons are observed, indicating that the transitions are not driven by conventional phonon softening.

However, phonon frequencies exhibit clear anomalies at the cubic-to-tetragonal and tetragonal-to-monoclinic transitions, highlighting strong phonon-lattice coupling.

Lattice anharmonicity systematically increases as symmetry is reduced, particularly in the monoclinic phase. This increase may not only result from structural distortions but could also be influenced by the emergence of spin-spin correlations below the cubic-to-tetragonal transition. The evolving magnetic correlations may modify interatomic potentials, enhancing anharmonic effects beyond what is expected from structural distortions alone.

Increased lattice anharmonicity can have broader implications, particularly in influencing thermal properties [30] and spin-lattice interactions [31]. In KIB, the observed phonon anomalies emphasize the strong coupling between lattice dynamics and spin degrees of freedom. Further studies, such as neutron scattering, could provide deeper insights into the extent of spin-phonon interactions and their role in shaping the physical properties of this material.

In summary, this study demonstrates how structural distortions in KIB strongly influence both spin and lattice dynamics, with spin-orbit coupling playing a central role in mediating these effects. EPR results highlight the emergence of spin-spin correlations well above T_N , indicating that lattice symmetry reduction enhances exchange interactions and spin-lattice coupling. Simultaneously, Raman scattering reveals that lattice anharmonicity systematically increases across structural transitions, suggesting a strong interplay between phonon dynamics and evolving spin correlations. These findings establish K_2IrBr_6 as a model system for studying coupled spin-lattice effects in SOC-driven materials. Future studies, such as neutron scattering, could further elucidate the microscopic mechanisms underlying these interactions and their broader implications for quantum materials.

Acknowledgments

This work is supported by a Core Research Grant from SERB and an INSPIRE Faculty Award from DST in India. We also acknowledge the FIST Grant (SR/FST/ETI/2020/628). S. Bhatia acknowledges her PhD fellowship from the CSIR. All authors acknowledge the experimental support from NRF and CRF at IIT Delhi and the Institute Instrumentation Centre at IIT Roorkee. K.S. thanks N. Khan for multiple scientific discussions on K_2IrBr_6 .

APPENDIX A: Raman active phonon modes in tetragonal and monoclinic phases

Table III and Table IV lists the phonon mode energies for the tetragonal and monoclinic phases.

Table III. Fourteen Raman Active modes at zone-center for Tetragonal phase at the critical Γ point.

Γ_{Raman}	$\omega_{\text{cal}} (\text{cm}^{-1})$	Γ_{Raman}	$\omega_{\text{cal}} (\text{cm}^{-1})$
A_{1g}	----	B_{2g}	110.78
E_g	----	E_g	111.28
E_g	37.99	B_{1g}	112.32
E_g	59.23	B_{1g}	189.09
B_{1g}	68.03	B_{2g}	189.49
E_g	73.20	A_{1g}	190.79
E_g	99.04	A_{1g}	222.67

Table IV. Twenty-four Raman Active modes at zone-center for Monoclinic phase at the critical Γ point.

Γ_{Raman}	$\omega_{\text{cal}} (\text{cm}^{-1})$	Γ_{Raman}	$\omega_{\text{cal}} (\text{cm}^{-1})$	Γ_{Raman}	$\omega_{\text{cal}} (\text{cm}^{-1})$
B_g	----	A_g	75.37	B_g	126.26
A_g	----	B_g	75.70	A_g	126.96
B_g	9.34	A_g	85.30	A_g	179.22
A_g	21.67	B_g	95.81	B_g	180.62
A_g	35.51	A_g	98.25	A_g	193.96
B_g	43.02	B_g	106.38	B_g	198.36
B_g	61.53	B_g	111.02	B_g	221.11
A_g	64.53	A_g	117.05	A_g	225.55

References

- [1] W. Witczak-Krempa, G. Chen, Y. B. Kim, and L. Balents, Correlated quantum phenomena in the strong spin-orbit regime, *Annu. Rev. Condens. Matter Phys.* **5**, 57 (2014).
- [2] G. Jackeli and G. Khaliullin, Mott insulators in the strong spin-orbit coupling Limit: From Heisenberg to a Quantum Compass and Kitaev Models, *Phys. Rev. Lett.* **102**, 017205 (2009).
- [3] Y. Noda, T. Ishii, M. Mori, and Y. Yamada, Successive Rotational Phase Transitions in $K_2\text{SeBr}_6$. I. Structure, *J. Phys. Soc. Japan* **48**, 1279 (1980).
- [4] R. L. Armstrong, Structural properties and lattice dynamics of 5d transition metal antiferromagnetic crystals, *Phys. Rep.* **57**, 343 (1980).
- [5] H. W. Willemsen, C. A. Martin, P. P. M. Meincke, and R. L. Armstrong, Thermal-expansion study of the displacive phase transitions in $K_2\text{ReCl}_6$ and $K_2\text{OsCl}_6$, *Phys. Rev. B* **16**, 2283 (1977).
- [6] L. Savary and L. Balents, Quantum spin liquids: a review, *Reports Prog. Phys.* **80**, 016502 (2016).
- [7] B. J. Kim, Hosub Jin, S. J. Moon, J.-Y. Kim, B.-G. Park, C. S. Leem, Jaeyun Yu, T. W. Noh, C. Kim et al., Novel $j_{\text{eff}}=1/2$ mott state induced by relativistic spin-orbit coupling in Sr_2IrO_4 , *Phys. Rev. Lett.* **101**, 076402 (2008).
- [8] Y. Singh and P. Gegenwart, Antiferromagnetic Mott insulating state in single crystals of the honeycomb lattice material Na_2IrO_3 , *Phys. Rev. B* **82**, 064412 (2010).
- [9] T. Dey, A. Maljuk, D. V. Efremov, O. Kataeva, S. Gass, C. G. F. Blum, F. Steckel, D. Gruner, T. Ritschel et al., Ba_2YIrO_6 : A cubic double perovskite material with Ir^{5+} ions, *Phys. Rev. B* **93**, 014434 (2016).
- [10] N. Khan, D. Prishchenko, Y. Skourski, V. G. Mazurenko, and A. A. Tsirlin, Cubic symmetry and magnetic frustration on the fcc spin lattice in $K_2\text{IrCl}_6$, *Phys. Rev. B* **99**, 144425 (2019).
- [11] Q. Wang, A. de la Torre, J. A. Rodriguez-Rivera, A. A. Podlesnyak, W. Tian, A. A. Aczel, M. Matsuda, P. J. Ryan, J.-W Kim, J. G. Rau, and K. W. Plumb, Pulling order back from the brink of disorder: Observation of a nodal line spin liquid and fluctuation stabilized order in $K_2\text{IrCl}_6$, *arXiv:2407.17559* (2024).
- [12] N. Khan, D. Prishchenko, M. H. Upton, V. G. Mazurenko, and A. A. Tsirlin, Towards cubic symmetry for Ir^{4+} : Structure and magnetism of the antiferromagnetic $K_2\text{IrBr}_6$, *Phys. Rev. B* **103**, 125158 (2021).
- [13] M. Majumder, F. Freund, T. Dey, M. Prinz-Zwick, N. Büttgen, Y. Skourski, A. Jesche, A. A. Tsirlin, and P. Gegenwart, Anisotropic temperature-field phase diagram of single crystalline $\beta\text{-Li}_2\text{IrO}_3$: Magnetization, specific heat, and ^7Li NMR study, *Phys. Rev. Mater.* **3**, 074408 (2019).
- [14] J. H. E. Griffiths and J. Owen, Complex hyperfine structures in microwave spectra of covalent iridium compounds, *Proc. R. Soc. London. Ser. A. Math. Phys. Sci.* **226**, 96 (1954).
- [15] L. Bhaskaran, A. N. Ponomaryov, J. Wosnitza, N. Khan, A. A. Tsirlin, M. E. Zhitomirsky, and S. A. Zvyagin, Antiferromagnetic resonance in the cubic iridium hexahalides $(\text{NH}_4)_2\text{IrCl}_6$ and

- K_2IrCl_6 , Phys. Rev. B **104**, 184404 (2021).
- [16] J. Khatua, Q. P. Ding, M. S. R. Rao, K. Y. Choi, A. Zorko, Y. Furukawa, and P. Khuntia, Magnetic properties of a spin-orbit entangled $J_{\text{eff}} = 1/2$ honeycomb lattice, Phys. Rev. B **108**, 054442 (2023).
- [17] J. Khatua, S. Bhattacharya, A. M. Strydom, A. Zorko, J. S. Lord, A. Ozarowski, E. Kermarrec, and P. Khuntia, Magnetic properties and spin dynamics in the spin-orbit driven $J_{\text{eff}} = 1/2$ triangular lattice antiferromagnet $Ba_6Yb_2Ti_4O_{17}$, Phys. Rev. B **109**, 024427 (2024).
- [18] B. J. Hales, Electron Paramagnetic Resonance (EPR) Spectroscopy, Encycl. Inorg. Chem. 1 (2008).
- [19] H. Han, L. Zhang, H. Lui, L. Ling, W. Tong, Y. Zou, M. Ge, J. Fan, C. Zhang, L. Pi & Y. Zhang, Electron paramagnetic resonance study of the f-d interaction in pyrochlore iridate $Gd_2Ir_2O_7$, Philos. Mag. **95**, 3014 (2015).
- [20] P. Warzanowski, M. Magnaterra, Ch. J. Sahle, M. Moretti Sala, P. Becker, L. Bohatý, I. Císařová, G. Monaco, T. Lorentz, P. H. M. van Loosdrecht, J. van den Brink and M. Grüninger, Spin-orbital-lattice entanglement in the ideal $j=1/2$ compound K_2IrCl_6 , Phys. Rev. B **110**, 195120 (2024).
- [21] P. W. Anderson and P. R. Weiss, Exchange narrowing in Paramagnetic Resonance, Rev. Mod. Phys. **25**, 269 (1953).
- [22] A. Najev, S. Hameed, A. Alfonsov, J. Joe, V. Kataev, M. Greven, M. Požek, and D. Pelc, Magnetic resonance study of rare-earth titanates, Phys. Rev. B **109**, 174406 (2024).
- [23] S. Lee, B. H. Kim, M. J. Seong, and K. Y. Choi, Noncubic local distortions and spin-orbit excitons in K_2IrCl_6 , Phys. Rev. B **105**, 184433 (2022).
- [24] P. Stein, T. C. Koethe, L. Bohatý, P. Becker, M. Grüninger, and P. H. M. Van Loosdrecht, Local symmetry breaking and low-energy continuum in K_2ReCl_6 , Phys. Rev. B **107**, 214301 (2023).
- [25] M. S. Senn, D. A. Keen, T. C. A. Lucas, J. A. Hriljac, and A. L. Goodwin, Emergence of Long-Range Order in $BaTiO_3$ from Local Symmetry-Breaking Distortions, Phys. Rev. Lett. **116**, 207602 (2016).
- [26] P. G. Klemens, Anharmonic decay of optical phonons, Phys. Rev. B **148**, 845 (1966).
- [27] J. Menéndez and M. Cardona, Temperature dependence of the first-order Raman scattering by phonons in Si, Ge, and α -Sn: Anharmonic effects, Phys. Rev. B **29**, 2051 (1984).
- [28] K. Sen, Y. Yao, R. Heid, A. Omoumi, F. Hardy, K. Willa, M. Merz, A. A. Haghighirad, and M. Le Tacon, Raman scattering study of lattice and magnetic excitations in CrAs, Phys. Rev. B **100**, 104301 (2019).
- [29] D. Samanta, A. Mazumder, S. P. Chaudhary, B. Ghosh, P. Saha, S. Bhattacharyya, and G. D. Mukherjee, Phonon anharmonicity and soft-phonon mediated structural phase transition in $Cs_3Bi_2Br_9$, Phys. Rev. B **108**, 054104 (2023).
- [30] J. Ding, J. L. Niedziela, D. Bansal, J. Wang, X. He, A. F. May, G. Ehlers, D. L. Abernathy, A. Said, A. Alatas, Y. Ren, G. Arya, and O. Delaire, Anharmonic lattice dynamics and superionic transition in $AgCrSe_2$, Proc. Natl. Acad. Sci. U. S. A. **117**, 3930 (2020).
- [31] V. Gnezdilov, Yu. Pashkevich, P. Lemmens, A. Gusev, K. Lamonova, T. Shevtsova, I. Vitebskiy, O. Afanasiev, S. Gnatchenko, V. Tsurkan, J. Deisenhofer, and A. Loidl, Anomalous optical phonons in FeTe chalcogenides: Spin state, magnetic order, and lattice anharmonicity, Phys. Rev. B **83**, 245127 (2011).